

PAPER • OPEN ACCESS

Detection of laser-induced damage using He–Ne laser reflective imaging technique

To cite this article: F Novák *et al* 2026 *J. Opt.* **28** 055401

View the [article online](#) for updates and enhancements.

You may also like

- [Laser damage phenomena relevant to the design and operation of an ICF laser driver](#)
H Bercegol, A Boscheron, J-M Di-Nicola et al.
- [Detection of laser damage to the surfaces of materials and coatings with the aid of an induced gas discharge](#)
Valerii A Astapenko and O E Sidoryuk
- [Comparison of simultaneous on-line optical and acoustic laser damage detection methods in the nanosecond pulse duration domain](#)
T Somoskoi, Cs Vass, M Mero et al.



PAPER

OPEN ACCESS

RECEIVED

26 September 2025

REVISED

13 March 2026

ACCEPTED FOR PUBLICATION

13 April 2026

PUBLISHED

6 May 2026

Original content from this work may be used under the terms of the [Creative Commons Attribution 4.0 licence](#).

Any further distribution of this work must maintain attribution to the author(s) and the title of the work, journal citation and DOI.



Detection of laser-induced damage using He–Ne laser reflective imaging technique

F Novák^{1,2,*} , L Uvarova¹ , Š Němcová^{1,3} and M-G Mureşan¹ ¹ HiLASE Centrum, Institute of Physics of the Czech Academy of Sciences, Dolní Břežany, Czechia² Faculty of Nuclear Sciences and Physical Engineering, Czech Technical University, Břehová 7, Prague, 115 19, Czechia³ Faculty of Mechanical Engineering, Czech Technical University in Prague, Technická 4, Prague, 166 07, Czechia

* Author to whom any correspondence should be addressed.

E-mail: frantisek.novak@hilase.cz**Keywords:** *in situ* damage detection, laser-induced damage threshold, He–Ne laserSupplementary material for this article is available [online](#)

Abstract

The reduction of laser-induced damage is a serious challenge for optical components; therefore, determining the laser-induced damage threshold (LIDT) is a crucial step in the manufacturing process. This article introduces a He–Ne laser imaging system designed for *in situ* damage detection within a LIDT station. The system provides fourfold-magnified imaging of the test sample and its surroundings, capturing the damage shape and size without requiring any imaging optics to be placed inside the vacuum chamber. This design helps maintain the cleanliness of the chamber. The detection method can be applied to both transparent and opaque samples; in transparent optics, the damage is observable from either side and it can be distinguished on which side the damage developed. To verify the system's functionality, two sample types were investigated: a silica wafer (non-transparent for He–Ne radiation) and a commonly used double-coated anti-reflective window at 1030 nm (transparent for He–Ne radiation). Particular attention was devoted to determining the minimum damage size that can be reliably recognized. The system successfully distinguished damage features as small as 35 μm .

1. Introduction

The study of the laser-induced damage threshold (LIDT) of optical materials plays an important role in areas such as research-grade laser optics (coating and thin-film research [1,2]), space/aerospace laser optics (the study and development of their properties according to space-related conditions [3–7]), and medicine (skin [8] or cornea laser thresholds [9]).

The LIDT of optical components is also becoming critical for high-energy high-power laser system development, especially for the improvement of anti-reflection/high-reflection (AR/HR) coatings of laser crystals [10], including active media and non-linear crystals, which are in general subjected to a higher fluence since the laser's efficiency is correlated with the pumping intensity. The same applies for the generation of higher harmonics, which is effectively achieved by high-intensity pumping [11].

One of the critical parts of the LIDT experiments is the *in situ* damage detection. Based on the large number of articles regarding LIDT tests, several methods of *in situ* damage detection are employed:

- long working distance microscopy [10, 12];
- fluorescence detection [13];
- scattered light monitoring [14, 15];
- plasma spark monitoring [16];

- online fast camera microscopy [17];

In many cases (i.e. for space applications) it is necessary to take the vacuum environment into account. Since the LIDT of materials can be dependent on the surrounding pressure, such studies are important. On the other hand, applying some conventional *in situ* damage detection methods under vacuum conditions may present difficulties. Therefore, for LIDT measurements in a vacuum, an efficient method of *in situ* damage detection is required. There are several limitations, such as the dimensions of the vacuum chamber or the difficulty of sample removal during the experiment. Thus, applying a He–Ne laser in reflection imaging mode for the *in situ* damage detection of samples was proposed.

The method of damage detection based on He–Ne laser light has been described in several articles [18–27]. Liu *et al* used a He–Ne gas CW laser at an angle of incidence (AOI) of 30° to detect the damage to the sample [18]. On the sample, the He–Ne laser beam had a diameter ($1/e^2$) of 1 mm, with the reflected beam directed to a power meter. The damage occurrence was indicated by a reduction in the reflected beam power. Yang *et al* [19] employed a He–Ne laser collinearly combined with a Nd:YAG laser. The method relied on the scattering of the He–Ne laser light from the damage. In addition, *in situ* He–Ne detection was used in several other articles [20–26], where damage detection was based on He–Ne laser scattering. Via scattering, the smallest detection limit was reached by Kafka *et al* [26] at under $1\ \mu\text{m}$.

In [27], Mikami *et al* utilized He–Ne laser imaging in a transmission setup, where the camera captured the fraction of He–Ne radiation transmitted through the sample to study the temperature dependence of the LIDT of single-layer coatings on silica glass substrates.

In [28], Mikami *et al* present a system in which a He–Ne laser, co-aligned with the laser inducing the damage, detects damage based on reflection at a 0° AOI with threefold magnification through a pair of lenses with focal lengths of 200 and 600 mm.

It is also worth mentioning the work of Bartels *et al* [29], who investigated the effect of laser conditioning on the LIDT of AR optics using a chopped He–Ne laser beam for *in situ* damage detection. In their setup, the He–Ne laser beam overlapped with the main UV laser beam used during the LIDT tests, and the scattered He–Ne light from the damage sites was detected by a Si photodiode. The authors concluded that they were able to detect damage down to $5\ \mu\text{m}$ in size.

An interesting work is the dissertation and paper [30, 31] by Avicé *et al*, in which a detection system using a He–Ne laser is described and constructed, based on the imaging of scattered light in the MISTRAL LIDT station. The He–Ne laser is expanded by a diverging lens onto the sample and illuminates it at a 45° angle. The reflected He–Ne beam is blocked by a diaphragm, while the light scattered from the damage is imaged by an XCD digital camera, also at a 45° angle. The system is noteworthy because it reveals the morphology of the damage using scattered light (dark-field technique) from both sides of the sample. Given the camera's pixel size of $19 \times 12.9\ \mu\text{m}^2$, the system can resolve damage on the scale of tens of micrometers.

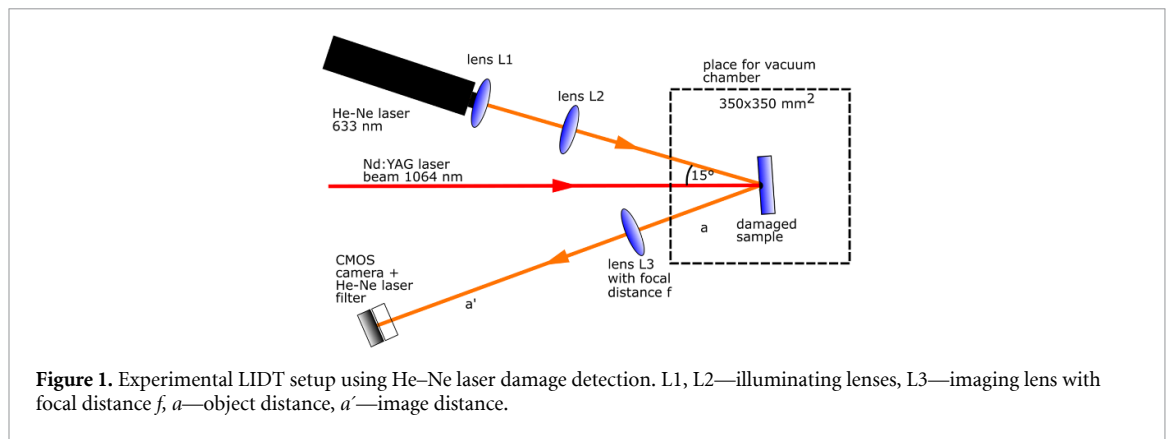
Interesting works in terms of *in situ*, real-time damage detection include the experimental studies by various authors in [32–37]. They describe two laser systems—the conditioning and damage setup at CEA/Ripault and the laser damage facility setup at the Fresnel Institute. The system at CEA/Ripault is interesting for its use of multiple surface-scanning detection methods, including absorption synchronous detection, scattering synchronous detection, and front-surface luminescence detection. A front-surface CCD camera is then used to detect the occurrence of damage. All these systems operate in real time. The laser damage facility at the Fresnel Institute employs a He–Ne laser collinear with the testing laser. The sample is observed in real time using an *in situ* optical microscope in different modes.

Based on the above-mentioned literature, both reflection- and transmission-based methods have been tested. It is concluded that reflected He–Ne light imaging detection is better suited for application in our case due to the simplicity and versatility of this method.

In this work, the setup for damage detection based on the reflection and imaging of the He–Ne laser radiation is presented. The process and methodology used for establishing the smallest *in situ* detectable damage using a He–Ne laser system is described in detail.

The advantages of the newly developed system lie in the combination of the following features:

- the ability to identify the damage shape and size, which is useful for adjusting test parameters during experiments, in contrast to scattering-based He–Ne detection systems;
- the capability to image a wide area around the tested site, enabling the detection of secondary or additional damage;



- the relative compactness and simplicity of the system;
- the possibility to use the detection system with non-transparent samples;
- the possibility to distinguish on which side the damage has developed on a transparent sample;
- reduced requirements for expensive optical components due to the non-collinear and independent optical paths of the He–Ne and damage-inducing laser.

2. Experiment

This section is dedicated to the description of the He–Ne detection system and the samples that were selected for these experiments—a silica wafer and a double-coated AR window at 1030 nm. Damage to the samples was either already created during earlier experiments or during the measurement by a q -switched Nd:YAG laser. All experiments were carried out at standard pressure and a temperature of 22 °C without a vacuum chamber or its window (no vacuum environment). During the measurements, the relative humidity ranged between 40% and 55%.

2.1. Experimental setup

The He–Ne laser damage detection system is shown in figure 1 (Zemax scheme in supplementary figure S1). The sample was irradiated by a He–Ne laser. Part of the radiation is reflected, passes through the lens L3, and falls onto a CMOS detector. The principle of the system is based on achieving a sufficient intensity contrast (at least 10%) between the damaged and undamaged areas of the sample. In the damaged area, a large amount of photons is scattered, resulting in the reduction of the laser intensity captured at the CMOS detector. L3 forms an image on the camera sensor; the magnification value depends on the relative positioning of L3 and the camera to the sample.

The sample was mounted in a metal holder, which was attached to two crossed translation stages enabling precise positioning of the samples during the set of experiments. The damage was induced by an Nd:YAG laser (Q-smart 450, Lumibird) operating at 1064 nm. The AOI of the Nd:YAG laser was set to 3° to prevent back-reflection into the laser cavity. The laser delivered pulses with energies of up to 0.5 J and a duration of 8.5 ns. A vacuum chamber will later be integrated into the LIDT station to enable testing under vacuum conditions, which is essential for evaluating space optics. Both the geometric dimensions and the spatial position of the vacuum chamber were taken into account during the design and implementation of the He–Ne detection system.

The He–Ne probe beam was aligned to overlap the Nd:YAG laser spot on the sample at an incidence angle of 15° relative to the Nd:YAG beam axis. Combined with the 3° AOI of the Nd:YAG laser, this configuration resulted in the He–Ne radiation interacting with the sample at an effective AOI of 18°. After reflection from the sample, the angle of the He–Ne beam to the Nd:YAG beam axis was 21°. The final value of the chosen angle was primarily determined by the construction of our vacuum chamber and the overall configuration of the individual elements of the LIDT station. The general objective was to achieve the smallest possible value of AOI in order to avoid potential undesirable optical phenomena on the vacuum chamber windows (such as astigmatism).

The core component of the imaging system was a linear S -polarized 632.8 nm He–Ne laser (HNLO50L, Thorlabs), continual, 5 mW with a beam diameter of 0.81 mm ($1/e^2$). The beam diameter at the sample plane could be changed by adjusting the distance between the two plano-convex lenses L1

($f = 60$ mm) and L2 ($f = 75$ mm)—for this work, the beam diameter at the sample plane was 11 mm ($1/e^2$) (both samples). A larger He–Ne beam diameter was used to image the damage and its surroundings, with a field of view given by the CMOS sensor size divided by the magnification factor of 4 and for the case of absence of motorized stages suitable for a vacuum environment (thus allowing the use of conventional motorized stages for the camera). Damage imaging was performed using a bi-convex lens (L3) and a CMOS camera (Beamage-3.0, Gentec) with a 2048×1088 pixel sensor with physical dimensions 11.3×6.0 mm² and a pixel pitch of 5.5×5.5 μm². The required distances between lens L3 and the sample (denoted a) and between lens L3 and the camera (denoted a') were calculated using the following equations to achieve the desired magnification:

$$\frac{1}{a} + \frac{1}{a'} = \frac{1}{f} \quad (1)$$

$$Z = -\frac{a'}{a} \quad (2)$$

where f denotes the focal length of the lens, a is the object distance, a' is the image distance, and Z is the magnification. In addition, a 632.8 nm bandpass filter was mounted in front of the CMOS camera to reduce noise. The He–Ne laser was chosen as the probe beam source because its wavelength differs from those of the Nd:YAG fundamental, second, and third harmonics. This spectral separation ensured that only the probe beam reached the sensor, effectively filtering out any residual radiation from the pump laser.

There are several limiting factors in our setup. The internal dimensions of the vacuum chamber are equal to $350 \times 350 \times 350$ mm³. The sample is located at its center. In order to minimize the number of optical elements inside the vacuum chamber, the lens L3 should be placed outside the chamber. Consequently, the distance between the sample and the imaging lens must be at least $(350/2) \times (1/\cos(21^\circ)) = 187$ mm.

The second limiting factor is the overall compactness of the setup. The distance between the sample and the camera must not exceed 1300 mm, as limited by the dimensions of the optical table. To achieve maximum magnification while respecting this spatial constraint, the lens L3 with a focal length of $f = 200$ mm was selected. As a result, a magnification of $|Z| = 4$ was reached, which means according to equation (1) a distance of $a = 250$ mm and consequently $a' = 1000$ mm. Lens L3 was mounted on a translation rail to achieve fine adjustment along the optical axis between the sample and the camera.

Based on the magnification $|Z| = 4$ and pixel size 5.5×5.5 μm², and assuming that effective noise suppression requires the dark spot area on the camera sensor to span at least five pixels in one dimension, a detection limit of about 7 μm for the smallest observable damage was established.

Another limiting factor of the detection system arises from Rayleigh's criterion for resolving two-point sources based on their diffraction patterns. The minimum resolvable feature of size r , on the surface of a tested component, in a diffraction-limited system is given by

$$r = 1.22 \frac{\lambda \cdot a}{D} \cong 4 \mu\text{m} \quad (3)$$

where $\lambda = 632.8$ nm is the wavelength of the probe beam, $a = 250$ mm is the distance between the sample and the imaging lens, and $D = 50.8$ mm is the aperture diameter of the lens. A potential improvement in resolution would be to use a lens with a shorter focal length, allowing the lens according to equation (1) to be placed closer to the sample, thereby reducing the value of a . However, this solution is restricted by the physical dimensions of the vacuum chamber, which limits the minimum achievable distance between the sample and the detection limit of the CMOS camera.

2.2. Samples

To verify the functionality of the detection setup and to determine the smallest detectable damage site, two samples were used: a silicon wafer with dimensions of 43×43 mm² and a thickness of 0.525 mm with one side polished, and a fused silica window with both sides anti-reflective coated (AR@1030 nm, AOI 0°). The diameter of the window was 1" (25.4 mm) and the thickness was 9 mm. A set of new damage was induced on both samples by the Nd:YAG laser. Based on the variation in the fluence and number of pulses, damage of various sizes was created.

The selection of these two samples was motivated by their differing optical properties. The refractive index of silicon at a wavelength of 632.8 nm is 3.87 [38]. The extinction coefficient of silicon at a wavelength of 632.8 nm is approximately 0.015 [38]. At an incidence angle of 18°, this results in a

reflectivity of approximately 37% for S-polarized light at the air–silicon interface; the remaining light is absorbed or scattered.

The AR double-coated window was highly transmissive at its design central wavelength of 1030 nm. However, for He–Ne laser radiation, the coated surfaces were partially reflective. In contrast to the silicon wafer, the absorption of He–Ne radiation in the fused silica is weak. As a result, a lateral-shearing interferogram is produced by the front- and back-surface reflections from a plane-parallel plate under oblique incidence. In this geometry, the expected fringes are straight and perpendicular to the direction of shear, in agreement with the classical single-plane-parallel-plate shearing interferometer. These interference fringes affect subsequent image processing.

Both samples had previously been damaged by laser exposure during earlier experiments. The laser-induced damage spots on both samples were spaced at regular intervals. These equidistant positions were used to aid the identification of the corresponding damage sites in the camera images. Nevertheless, both samples still contained sufficiently large undamaged areas suitable for inducing new, controlled laser damage.

New laser-induced damage sites were also identified during detection based on their relative positions, determined from the LIDT test parameters for similar samples in the past—specifically, the fixed spacing between individual sites. Additionally, the identification process was aided by reference damage marks presented on each sample. Measurements of the damage morphology were conducted using a confocal microscope (OLS5000, Olympus).

3. Results of experiments and discussion

This section presents the experimental results of the *in situ* detection using a He–Ne laser on a silicon wafer and an AR window, both in real-time and non-real-time modes. For the silicon wafer, only non-real-time *in situ* detection was carried out, while for the AR window both real-time and non-real-time detection were applied. In the non-real-time case, two different configurations were used for the AR window, depending on which side the damage occurred. The detectability of the damage was evaluated by a human observer and by comparing horizontal intensity profiles taken at the center of the damaged location and at an undamaged region using image processing. The profile of the undamaged area was taken, in the case of *in situ* non-real-time measurements, from a region near the damage but outside the visible contamination. In the case of *in situ* detection in real time, the profile was taken in the exact same area before and after damage initiation. Multiple profiles were used for the comparison, and their data were subsequently averaged. Automatized computer-based image analysis of the CMOS camera data will be addressed in future work.

For smaller damage sizes, there is a risk of misidentifying the damage as a dust particle or another form of contamination. In the case of *in situ* real-time measurements, such confusion can be excluded by comparing images taken before and after laser irradiation. However, for *in situ* non-real-time measurements, this comparison is not possible. Nevertheless, the known positions of the damage sites can be used for identification since the sites are arranged at equidistant intervals. Furthermore, the origin of a given image feature can be verified by slightly translating the sample: the image of a dust particle on the optical components with the exception of the tested sample itself will remain stationary, whereas the image of an actual damage site will shift together with the sample. This method, however, does not apply to dust particles located directly on the sample surface because our facility was not in a clean room.

3.1. Damage detection on silicon wafer sample

On the silicon wafer sample, 22 new laser damage sites of various sizes were created and analyzed (figure 2), along with six pre-existing damage sites from earlier experiments, as summarized in supplementary table S1 (important spots in table 1). Some of the damage in figure 2 is barely visible because of its small dimensions and the absence of the colored surrounding area. The new damage was created using the Nd:YAG laser focused by a lens with a focal length of $f = 500$ mm. The beam exhibited a near-Gaussian spatial profile with a diameter of $167\text{ }\mu\text{m}$ (at $1/e^2$) at the sample surface, an ellipticity of 97% (see supplement figure S2). An attenuator was used to control the YAG laser fluence. Fluence levels were selected based on prior LIDT testing of similar samples. The resulting damage size depended on both the laser fluence and the number of pulses delivered. The six additional damage sites originating from earlier experiments were also created using the same Nd:YAG laser at the same LIDT station with a different lens focal length.



Figure 2. Silicon wafer sample map of the newly created damage sites (captured by confocal microscopy). Some of the damage is hardly observable because of the absence of the typical colored area surrounding the damage.

Table 1. List of important spots studied during the experiments with He–Ne laser detection and their parameters by the silica wafer sample. Spots 10 and 21 were newly damaged, while spots 25 and 26 were previously damaged. The dimensions of damage are denoted by Δx and Δy .

Spot #	Fluence (J cm ⁻²)	Pulses	Δx (μm)	Δy (μm)	He–Ne detection
10	3.6	100	165	155	yes
21	3.0	250	60	55	yes
25	—	—	35	30	yes
26	—	—	5	10	no

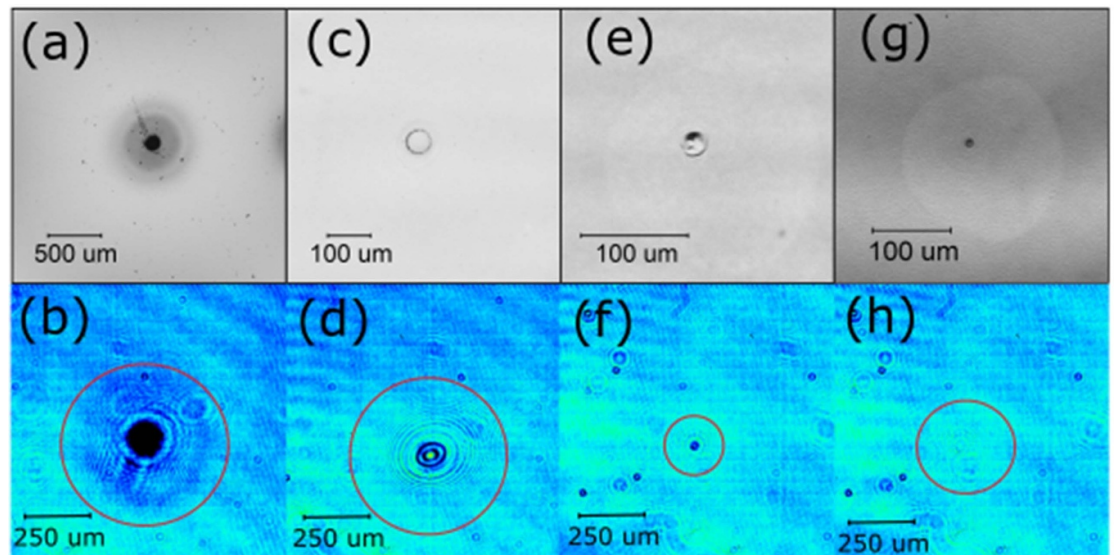


Figure 3. Damage at spots 10 (a) and (b), 21 (c) and (d), 25 (e) and (f), and 26 (g) and (h) of the silicon wafer sample as captured by confocal microscopy and CMOS camera under He–Ne laser illumination, respectively.

The smallest damage created using a fluence of 3.0 J cm⁻² had dimensions of 60 × 55 μm^2 (spot 21). From the previously tested sites, damage with dimensions of 35 × 30 μm^2 (spot 25) and a smaller one of 5 × 10 μm^2 (spot 26) were included in this work.

As shown in table 1 and supplementary table S1, the He–Ne detection setup successfully detected damage at all locations except for the smallest site (spot 26).

Figure 3(a) presents a typical damage site (spot 10) induced by the Nd:YAG laser, with dimensions of 165 × 155 μm^2 . Its corresponding He–Ne image in figure 3(b) reveals morphological features surrounding the damaged region. Figure 3(c) presents the smallest damage produced using 3.0 J cm⁻² fluence. The corresponding He–Ne detection is shown in figure 3(d). Figures 3(e) and (f) show the damage in spot 25—the smallest detectable damage with dimensions 35 × 30 μm^2 . The tiny amount of damage on spot 26 can be seen in figure 3(g). Only a weak diffraction pattern was visible at the location of spot 26 (see figure 3(h)) when using He–Ne detection.

Figure 4 shows a comparison of the intensity profiles taken. As can be seen in figure 4(d) at spot 26, no sufficient difference between the profile of the damaged and undamaged area can be observed; therefore, no detection is stated. Therefore, the smallest detected damage on the silicon sample was 35 × 30 μm^2 .

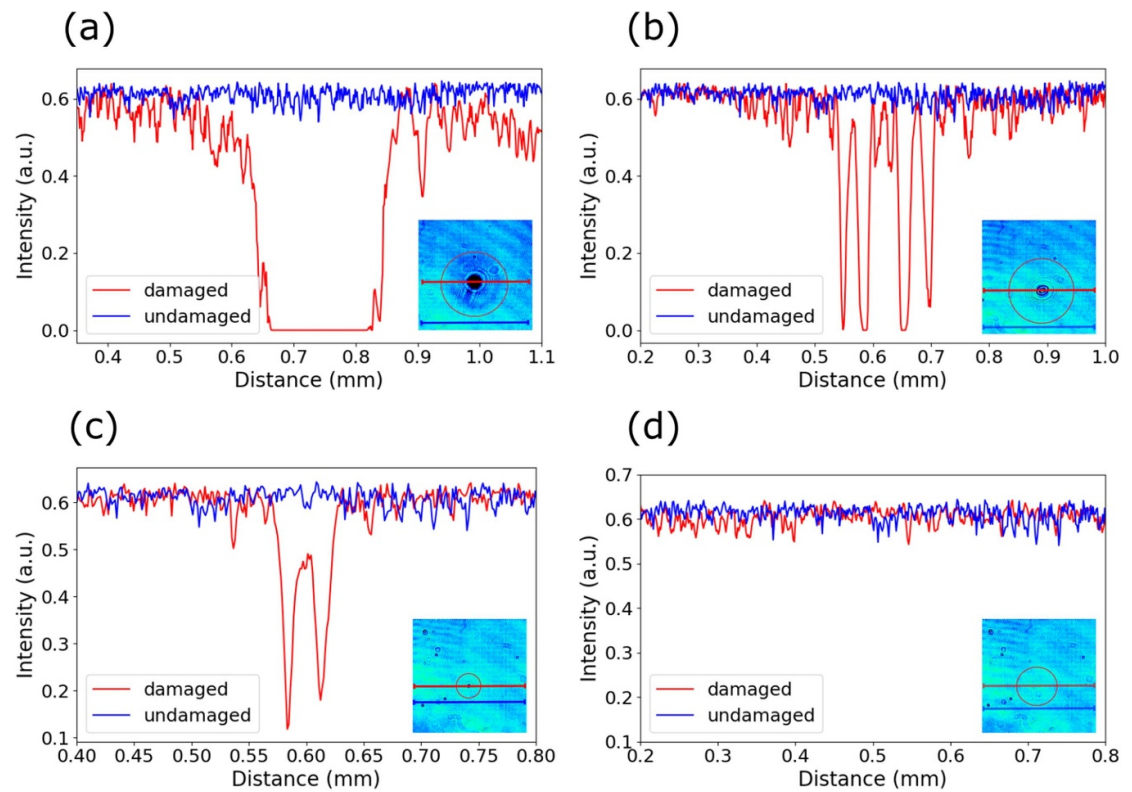


Figure 4. Intensity horizontal profiles of the damages at spots 10 (a) and (b), 21 (b), 25 (c), and 26 (d) of the silicon wafer sample as captured by CMOS camera under He–Ne laser illumination.

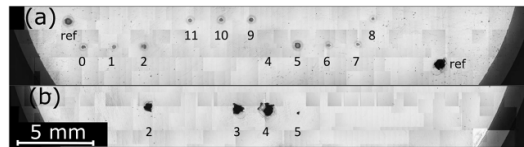


Figure 5. Map of the damaged spots in the (a) S1 and (b) S2 side of the AR window newly created by Nd:YAG laser (captured by confocal microscopy).

3.2. Damage detection on AR window

As with the silicon wafer sample, both newly induced and previously existing damage sites were analyzed on the AR window. A total of 12 new damage sites were created by a Nd:YAG laser (see figure 5). The beam exhibited the same parameters as for the silicon wafer (a near-Gaussian spatial profile with a diameter of $167\ \mu\text{m}$ ($1/e^2$) at the sample, an ellipticity of 97%). The laser beam was focused on the S1 side - Side S1 denotes the laser-incident surface. In four cases (spots 2, 3, 4, and 5), damage was also observed on the S2 side.

The smallest recorded damage occurred at a fluence of $76.7\ \text{J cm}^{-2}$ with 10 pulses in spot 4 (on S1), resulting in dimensions of $50 \times 35\ \mu\text{m}^2$. With the exception of spot 5, all S2-side damage sites exhibited larger lateral dimensions than those on the S1 side. In addition, two complex damage sites from previous experiments were analyzed to verify the detection capabilities of the system (see figures 7(e) and (g)). This damage was created using the BIVOL laser system (flat top spatial profile, 1030 nm, 2–14 ns, energy up to 7 J). The details regarding the BIVOL laser system and the LIDT testing procedure used were previously published [39, 40].

As with the silicon wafer, damage detection using the He–Ne probe laser was performed *in situ*, but not in real-time mode. However, unlike in the case of the silicon wafer, detection was performed in two distinct configurations, realized by flipping the sample within the holder:

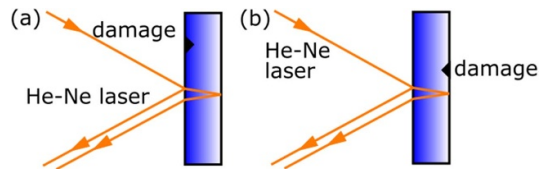


Figure 6. Damage detection setups used for the transparent optics: (a) damage on the front side (DFS) and (b) damage on the rear side (DRS).

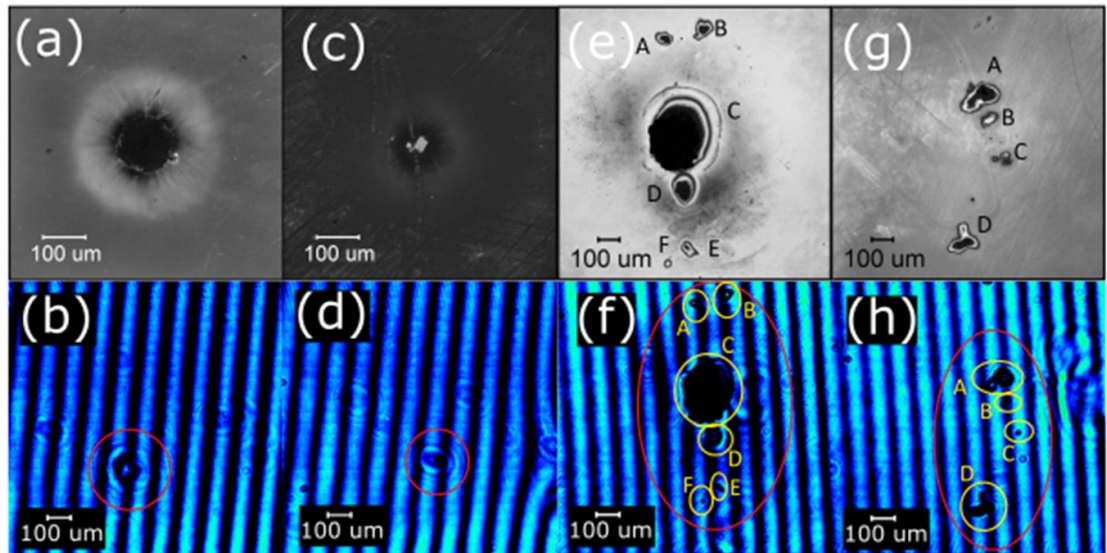


Figure 7. Damage at spots 8 (a) and (b), 4 (c) and (d), 12 (e) and (f), and 13 (g and h) of the AR window captured by confocal microscopy and CMOS camera under He–Ne laser illumination, respectively, in DFS configuration.

- Damage on the front side (DFS): the He–Ne beam was incident from the same side where the damage occurred.
- Damage on the rear side (DRS): the He–Ne beam was incident from the opposite side to where the damage occurred.

This two-configuration approach was motivated by the fact that during LIDT testing, laser-induced damage may also occur on the rear surface of the sample—opposite to the laser entry side (figure 6). All results from the He–Ne laser-based detection and the corresponding damage parameters are summarized in supplementary table S2 (important spots in table 2). For the fromDFS configuration, the damage captured by the confocal microscope and the images at the CMOS camera are depicted in figure 7. A typical damage site created at a fluence of 42.8 J cm^{-2} is shown in figure 7(a). The damage shape closely follows the Gaussian profile of the laser beam, with an approximate diameter of $135 \mu\text{m}$. The corresponding He–Ne laser image is shown in figure 7(b), where the previously discussed interference pattern (arising from reflections on both the S1 and S2 sides) is clearly visible. Based on the image analysis, the average spacing between interference maxima is approximately $550 \mu\text{m}$, while the average width of the destructive interference band (i.e. the dark fringe) is about $170 \mu\text{m}$. Considering that the imaging system provides a magnification of $|Z| = 4$, this implies that the detection of damage smaller than approximately $170 \mu\text{m} / 4 \approx 40 \mu\text{m}$ may be random. The smallest laser-induced damage observed during the experiments is shown in figure 7(c) and its corresponding He–Ne image in figure 7(d) (spot 4). Rear-side damage is visible in the right part of figure 7(d), where it is revealed as a localized disturbance or compression of the interference field. Figures 7(f) and (h) present complex damage structures from earlier experiments. In both cases, the damaged regions are clearly recognizable. For spots 12F and 13C, however, it remains uncertain whether such damage would remain visible if it was located within a region of destructive interference. Therefore, the smallest reliably detectable damage under the given imaging conditions was $50 \times 30 \mu\text{m}$. The intensity profile comparison of the smallest damage (spot 13B) is depicted in figure 8.

Table 2. List of important spots studied during the experiments with He–Ne laser detection and their parameters by the AR window. Spots 0–11 were newly damaged, while spots 12–13 were previously damaged. The detection column indicates whether the damage is detected in the DFS setup or in the DRS setup. The dimensions of the damage are denoted by Δx and Δy . Side S1 denotes the laser-incident surface.

Spot #	Fluence (J cm^{-2})	Pulses	Δx (μm)	Δy (μm)	Damaged side	He–Ne detection	
						DFS setup	DRS setup
0	49.3	10	160	145	S1	yes	no
4	76.7	10	50/445	35/605	S1 + S2	yes + yes	no + yes
7	42.8	100	105	115	S1	yes	yes
8	42.8	50	130	135	S1	yes	yes
11	58.1	20	150	165	S1	yes	yes
12A	—	—	70	40	S1	yes	yes
12B	—	—	55	50	S1	yes	yes
12C	—	—	250	320	S1	yes	yes
12D	—	—	80	100	S1	yes	yes
12E	—	—	45	50	S1	yes	yes
12F	—	—	35	40	S1	yes	no
13A	—	—	130	85	S1	yes	yes
13B	—	—	50	30	S1	yes	no
13C	—	—	30	25	S1	yes	no
13D	—	—	95	40	S1	yes	yes

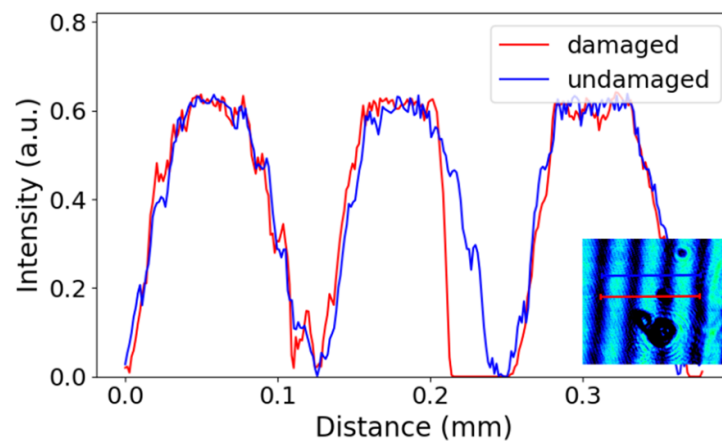


Figure 8. Intensity horizontal profiles of the damage at spot 13C of the AR window sample as captured by CMOS camera under He–Ne laser illumination in DFS configuration.

In the DFS configuration, the damage appears as a dark region within the interference field, as it scatters light reflected from both sides. In contrast, in the DRS configuration, light reflected from the front side is unaffected by damage, because the damage is on the rear side. Instead, the damage is revealed as a local disturbance of the interference pattern. Disruptions in the regularity of the interference fringes are more easily detectable and, moreover, more readily analyzable by software. This also addresses the potential problem of failing to detect damage located at an interference minimum, as can occur in the DFS configuration. This may be considered as a benefit of using coherent probe radiation (for instance, coherent light is the basis of an electronic speckle pattern interferometry technique, which is used for material defect detection [41]). An additional advantage of employing coherent radiation is the possibility of identifying whether the damage is situated on the front or back side based on the image of the damage. However, in general, better configuration depends mainly on the type of coating on the front and rear side. It is also important to consider that if damage occurs at corresponding positions on both the front and rear surfaces, the rear-side damage image will appear laterally shifted relative to the front-side damage image due to geometric optical effects. Therefore, the AOI of the laser beam must be selected carefully to avoid spatial overlap between rear-side and front-side damage—particularly when these are produced at regular intervals. In the experiment, this spatial displacement caused the damage at spot 0 (near the edge of the sample) to go undetected because the shifted image of the rear-side damage fell within a region obscured by the mechanical sample holder. The holder has a thickness of 7 mm and encloses the sample along its perimeter. This fact caused together with the thickness of

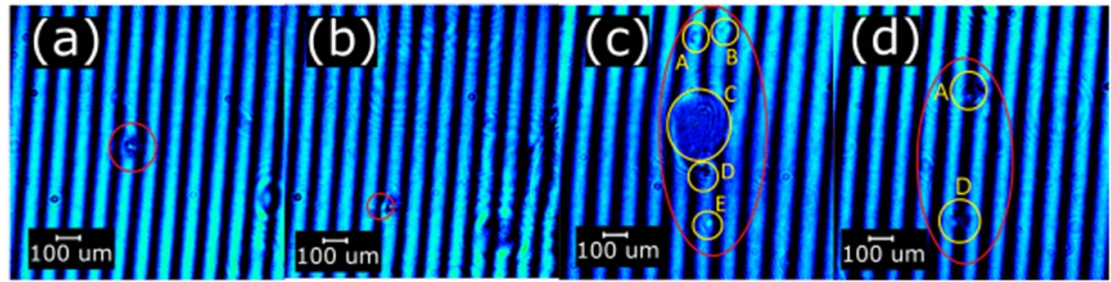


Figure 9. Damage at spots 8 (a), 4 (b), 12 (c), and 13 (d) of the AR window illuminated with He–Ne laser on CMOS camera in DRS configuration.

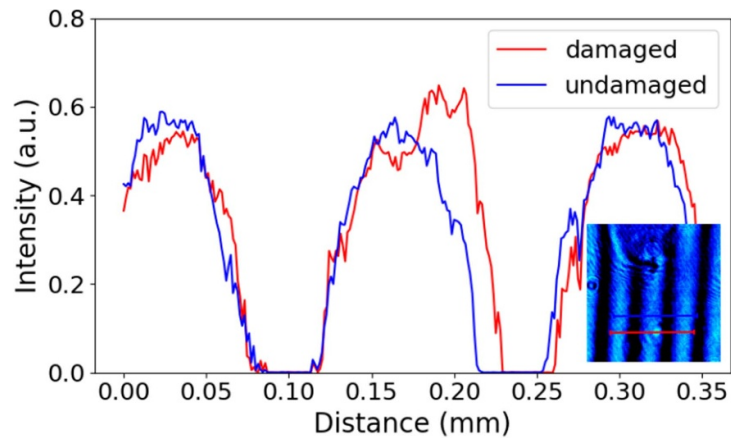


Figure 10. Intensity horizontal profiles of the damages at spot 12E of the AR window sample as captured by CMOS camera under He–Ne laser illumination in DRS configuration.

the sample 9 mm that the reflected beam was blocked by the holder and did not reach the detection system. An improved sample holder will be used in future experiments to prevent this type of overlap. A potential long-term solution is to design a holder that supports only a part of the sample rather than surrounding it entirely, ensuring that the optical path of the reflected He–Ne beam remains unobstructed. The damage site at spot 8 (marked by a red circle) is shown in figure 9(a) as a representative example of damage at the S1 side imaged using the DRS detection setup. The damage is visible as a disruption of the interference field. In contrast, the detection of the $50 \times 35 \mu\text{m}$ damage at spot 4 (also S1-side damage) was debatable in the DRS configuration. Figures 9(c) and (d) present complex damage sites. In the case of spot 12, multiple damage sites (A–E) can be clearly identified. For spot 13, only damage sites 13A and 13D are recognizable. Among all identified sites, spot 12E represents the smallest reliably detectable damage, with dimensions of $45 \times 50 \mu\text{m}$ (see figure 10 for an intensity profile comparison). Therefore, the smallest reliably detectable damage size in the DRS configuration can be estimated at approximately $50 \mu\text{m}$, which is comparable to the detection threshold observed in the DFS configuration. The smallest induced damage site reliably detected in this configuration was spot 7, with dimensions of $105 \times 115 \mu\text{m}$ (see figure 11(b)).

3.3. *In situ* damage detection in real time

In situ real-time damage detection was performed only on the AR window during LIDT testing, as described above. As previously noted, *in situ* detection in real time offers the advantage of allowing direct comparison between images recorded before and after laser exposure. This contrast significantly improves damage identification. Figures 12(a) and (b) show spot 7 before and after the laser shot. In figure 12(c) there is clearly observed damage, based on the subtraction of figures 12(a) and (b). The improvement of the detectability can also be seen in the intensity profile comparison—see figures 13 and 14. A limitation of *in situ* real-time detection, however, is the inability in some cases to predict which surface of the sample (front or rear) will be damaged. Because only one surface can typically be imaged in focus, damage on the opposite side may not be clearly resolved. This effect has to be taken

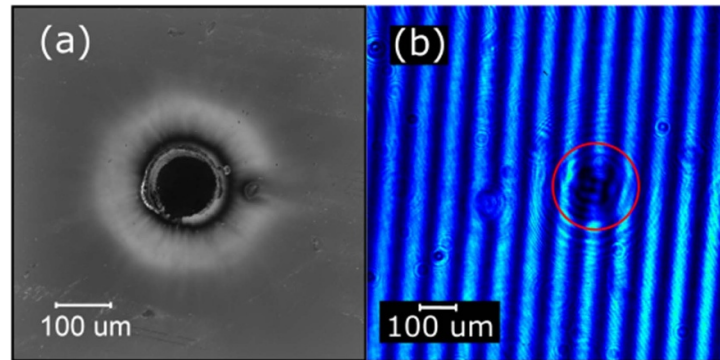


Figure 11. Damage at spot 7 of the AR window as captured by confocal microscopy (a) and CMOS camera under He–Ne laser illumination, respectively (b).

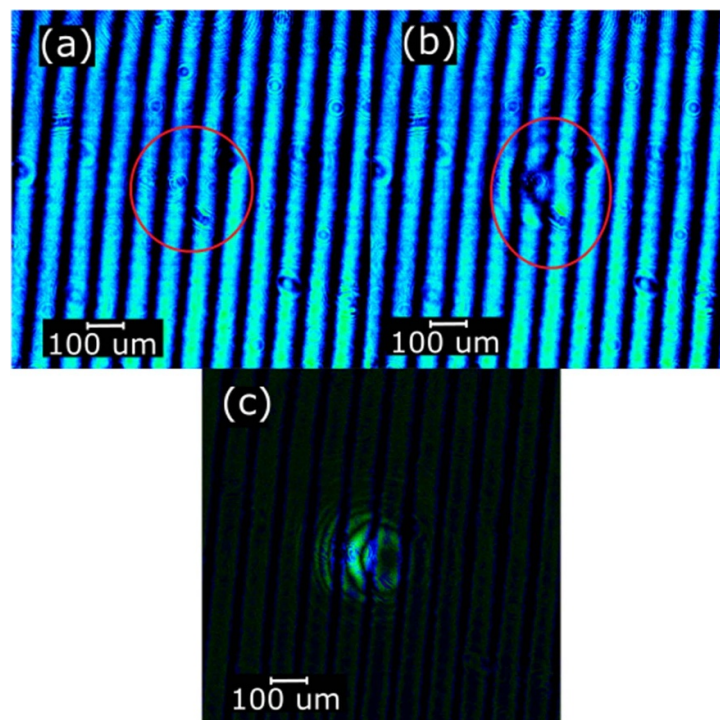


Figure 12. He–Ne laser detection image of spot 7 of AR window before (a) and after (b) damage creation, and (c) on subtraction of the images.

into account during real-time detection, but it can be overcome by a sufficiently high depth of field of the imaging optics.

Automated image analysis based on frame differentiation is one of the aims of future studies.

3.4. Discussion

A fundamental restriction arises for samples that do not sufficiently reflect light at the He–Ne laser wavelength; for instance, materials that appear ‘black’ to the human eye used in the production of astronomical instruments [42]. For such materials, different acceptable wavelengths can be applied within the same detection system configuration.

The obvious problem in the case of DFS configuration is interference fringes. The interference fringes are caused by the curved wavefront of the incident He–Ne laser radiation. The interference structure can be tuned mainly by changing the beam divergence by adjusting the positions of lenses L1 and L2 or by changing their parameters. In the current setup, an improvement could be achieved by inserting a rotating wedged silica plate, which does not suppress the interference but allows control over the positions of the interference fringes.

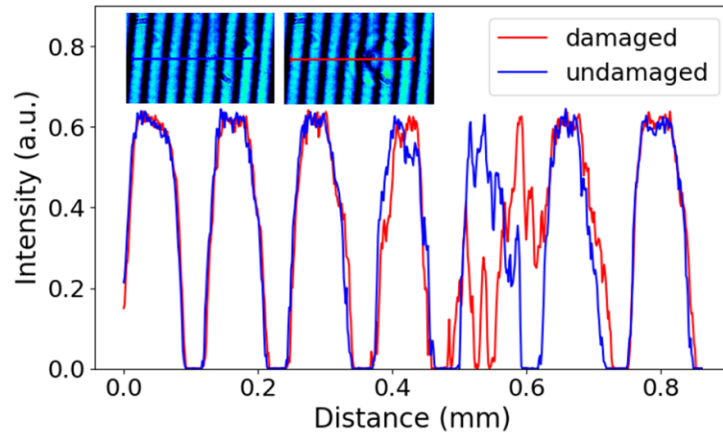


Figure 13. Intensity horizontal profiles at spot 7 of the AR window sample as captured by CMOS camera under He–Ne laser illumination during *in situ* damage detection.

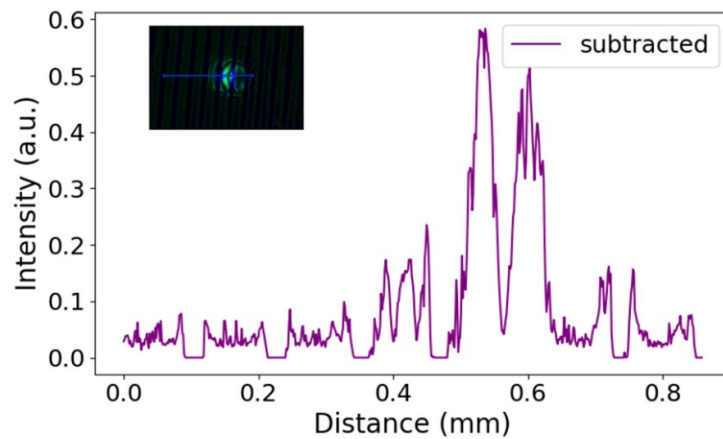


Figure 14. Intensity horizontal profiles of the damage at spot 7 of the AR window sample as captured by CMOS camera under He–Ne laser illumination during *in situ* damage detection in real time after subtracting figures 12(a) and (b).

With our method, the smallest detected damage size for the silicon wafer was $35 \times 30 \mu\text{m}^2$. A $5 \times 10 \mu\text{m}$ defect could not be detected, most likely due to limitations of the camera (pixel size), but other factors also play a role. First, the shallow depth and inherently weak contrast of such small defects reduce their visibility. In addition, interference effects caused by contamination, dust, laser speckle (an interference pattern arising from microscopic surface roughness or refractive index variations), and other surface imperfections may further degrade the intensity contrast, rendering the smallest damage sites undetectable. The detection performance may also have been affected by the standard laboratory environment in which the experiment was performed. Last but not least, the intensity contrast is also influenced by the optical coating itself, which affects how much radiation is reflected from the front or back side of the sample.

Improved contrast could also be achieved by introducing a spatial filter between lenses L1 and L2, which can reduce the fine interference fringes observed on the silica wafer sample.

Using a single-element imaging lens (L3; $\text{Ø}50 \text{ mm}$, $f = 200 \text{ mm}$, i.e. $f/4$) inevitably limits the image quality and thus the achievable resolution. At $f/4$, the dominant residual aberration is expected to be spherical aberration, while coma and astigmatism should remain negligible due to the small field angle ($\sim 0.3^\circ$). Since no chamber window was used, no additional astigmatism was introduced.

As mentioned earlier, higher magnification could be achieved if the imaging lens was positioned inside the chamber; alternatively, the same lens could provide higher magnification by increasing the distances a and a' . However, this would imply operating with a larger beam incident on the imaging lens and a larger a' , which would conflict with the compactness requirements of the setup. When reducing the distance a , care must be taken to ensure that the Nd:YAG laser beam does not touch the L3 lens

holder. It can therefore be stated that, considering the compactness of the system and keeping the L3 lens outside the vacuum chamber, the chosen single-lens geometric arrangement was optimal.

Another important limitation arises from the resolution of the CMOS camera and the diffraction limit given by the Rayleigh criterion. Nevertheless, future improvements are expected to push these limits and enable detection of even smaller damage features. A possible solution for the future could be the addition of a scattered-light detection system. In combination with the presented system, this could lead to increased detection efficiency. An LIDT station with multiple detection systems is described, for example, in articles [32–37]. The last improvement could be done through the use of a camera with smaller pixel dimensions.

The highest contrast of fringes is when the polarization of the interfering beams is the same. The polarization after the interaction with the sample will be preserved for an S-polarized beam—this is beneficial for the DRS configuration. To improve detection in the DFS configuration, using an unpolarized He–Ne laser could be beneficial.

In the work [27], the author utilized He–Ne laser imaging in a transmission setup, where the camera captured the fraction of He–Ne radiation transmitted through the sample. Compared to the reflection configuration, the transmission configuration does not offer the advantage that detection can be performed on both opaque and transparent samples.

Overall, *in situ* detection methods based on scattered He–Ne light appear to be capable of the detection of smaller damage sizes (e.g. $<1\ \mu\text{m}$ [26] and $5\ \mu\text{m}$ [29]). However, these methods provide only limited information on the damage shape and size. They also carry the risk of misinterpreting contamination particles as damage, and do not allow effective imaging of broader sample areas.

Compared to detection systems based on the energy decrease [18] and light scattering [20–26, 29], which detect the presence of damage, our system enables the visualization of the damage shape and size, as well as the damage surroundings. The reliable detection of damage *in situ*, especially for restricted access experiments, combined with the damage shape and size details, decides the further fluence selection in order to obtain the closest possible information of the LIDT parameters. Such techniques can be used to incrementally select the appropriate fluence levels for the test, and thus improve the accuracy of the experimental results. Moreover, although scattering-based detection provides only qualitative information, it cannot indicate the degree of damage, and often fails to reveal whether additional damage has formed in the surrounding area.

Furthermore, in the systems described in [21, 22, 24, 25, 27–29], the He–Ne laser is collinear with the laser that induces damage. Aligning the He–Ne beam with the laser that induces damage increases the demands on the optical components, both in terms of their LIDT and the need for additional AR/HR coatings, which complicates the manufacturing and replacement processes.

The work in [28], like the system presented here, is based on the reflection of a He–Ne laser. It is followed by a threefold telescopic magnification. However, the systems differ substantially in the (non-)alignment of the He–Ne laser with the laser inducing damage. A deeper comparison is not feasible, as the goals of this article and [28] are fundamentally different (LIDT dependence on temperature), and therefore we are not describing the detection system in detail.

The systems described in [21, 22, 24, 25, 27, 29] are, due to their design, applicable only to transparent samples, whereas our system is suitable for both transparent and non-transparent samples. In the case of transparent optics, damage can be observed regardless of the side on which it occurs.

The work of Avice *et al* [30, 31], based on imaging damage using scattered light, could also represent a potential alternative for this system in the future. The dark-field imaging system constructed by Avice provides good results and, unlike most scattered-light detection systems, also reveals the morphology of the damage. This system represents one possible approach for future work. Its implementation for LIDT measurements in a vacuum still needs to be tested.

4. Summary

In this work, the setup for damage detection based on the reflection and imaging of He–Ne laser radiation is presented. To assess the system's performance, two types of samples were tested: a silicon wafer and an AR window. For the silicon wafer, from the available set of damage spots, the minimum detectable size was $35 \times 30\ \mu\text{m}^2$. In the case of the AR window, two detection configurations were tested: DFS and DRS, which differed by the position of the damage relative to the incident He–Ne laser radiation. The smallest reliably detectable damage size was found to be $50 \times 30\ \mu\text{m}^2$ in the DFS and $45 \times 50\ \mu\text{m}^2$ in the DRS configuration, respectively.

Acknowledgments

This work was co-funded by the European Union and the state budget of the Czech Republic under the Project LasApp CZ.02.01.01/00/22_008/0004573.

The authors would like to thank Pavel Crha (HiLASE Engineering and Technical Support) for his contribution during the setup realization, designing and manufacturing custom mechanics.

Data availability statement

All data that support the findings of this study are included within the article (and any supplementary files).

Supplementary Material 1 available at <https://doi.org/10.1088/2040-8986/ae5e8c/data1>.

Supplementary Material 2 available at <https://doi.org/10.1088/2040-8986/ae5e8c/data2>.

Supplementary Material 3 available at <https://doi.org/10.1088/2040-8986/ae5e8c/data3>.

Conflict of interest

The authors declare that they have no known competing financial interests or personal relationships that could have appeared to influence the work reported in this paper.

ORCID iDs

F Novák  0009-0007-2332-3952

L Uvarova  0000-0003-1448-0642

Š Němcová  0000-0002-4260-0907

M-G Mureşan  0000-0002-1542-7416

References

- [1] Wang Y, Cheng X, Shao J, Zheng C, Chen A and Zhang L 2022 The damage threshold of multilayer film induced by femtosecond and picosecond laser pulses *Coatings* **12** 251
- [2] Velpula P K, Kramer D and Rus B 2020 Femtosecond laser-induced damage characterization of multilayer dielectric coatings *Coatings* **10** 603
- [3] Cao J, Chen T, He H, Xu Y, Chen Y, Gao N, Du Y, Wu Z and Liu Y 2023 Visible light performance of x-ray filters for Einstein *Opt. Eng.* **62** 044103
- [4] Weßels P, Büttner A, Ernst M, Hunnekuhl M, Kalms R, Willemsen L, Kracht D and Neumann J 2018 UV-DPSS laser flight model for the MOMA instrument of the exoMars 2020 mission *Proc. SPIE* **11180** 111801B
- [5] Riede W, Schroeder H, Bataviciute G, Wernham D, Tighe A, Pettazzi F and Alves J 2011 Laser-induced contamination on space optics *Proc. SPIE* **8190** 81901E
- [6] Wernham D, Alves J, Pettazzi F and Tighe A P 2010 Laser-induced contamination mitigation on the ALADIN laser for ADM-Aeolus *Proc. SPIE* **7842** 394–405
- [7] Sheng C Y 2006 Effects of laser-induced damage on optical windows in the presence of adhesives under simulated thermal-vacuum conditions *Proc. SPIE* **6403** 167–78
- [8] Jean M and Schulmeister K 2021 Laser-induced injury of the skin: validation of a computer model to predict thresholds *Biomed. Opt. Express* **12** 2586–603
- [9] Jean M, Schulmeister K, Lund D J and Stuck B E 2021 Laser-induced corneal injury: validation of a computer model to predict thresholds *Biomed. Opt. Express* **12** 336–53
- [10] Wang H, Meadows A R, Jankowska E, Randel E, Reagan B A, Rocca J J and Menoni C S 2020 Laser induced damage in coatings for cryogenic yb:YAG active mirror amplifiers *Opt. Lett.* **45** 4476–9
- [11] Chen J, Lin H, Hao D, Tang Y, Yi X, Zhao Y and Zhou S 2019 Exaggerated grain growth caused by ZrO₂-doping and its effect on the optical properties of Tb₃Al₅O₁₂ ceramics *Scr. Mater.* **162** 82–85
- [12] Neaupout J, Bonod N, Hocquet S, Palmier S and Dupuy G 2010 Mixed metal dielectric gratings for pulse compression *Opt. Express* **18** 23776–83
- [13] Schröder H, Riede W, Reinhold E, Wernham D, Lien Y and Kheyrandish H 2007 In situ observation of UV-laser-induced deposit formation by fluorescence measurement *Proc. SPIE* **6403** 512–22
- [14] Willemsen T et al 2022 Large area ion beam sputtered dielectric ultrafast mirrors for petawatt laser beamlines *Opt. Express* **30** 6129–41
- [15] Fourmaux S and Kieffer J 2021 Laser induced damage threshold and incubation effects of high-power laser system optics *Quantum Electron.* **51** 751
- [16] Nassef O A and Elsayed-Ali HE 2005 Spark discharge assisted laser induced breakdown spectroscopy *Spectrochim. Acta B* **60** 1564–72

- [17] Liu G and Kuang D 2024 Damage mechanism in plasma evolution of nanosecond laser-induced damage of germanium sheets in air and vacuum *Opt. Laser Technol.* **174** 110689
- [18] Liu G, Kuang D, Song L, Xu C and Yan C 2023 Mechanism in damage variation of nanosecond laser-induced damage of germanium sheets in vacuum *Opt. Laser Technol.* **157** 108663
- [19] Yang L, Xiang X, Miao X, Li Z, Li L, Yuan X, Zhou G, Lv H and Zu X 2015 Influence of oil contamination on the optical performance and laser induced damage of fused silica *Opt. Laser Technol.* **75** 76–82
- [20] Lien Y, Reinhold E, Wernham D, Endemann M, Jost M, Armandillo E, Riede W, Schröder H and Allenspacher P 2006 Risk mitigation in spaceborne lasers *Proc. SPIE* **6190** 9
- [21] Riede W, Allenspacher P and Wernham D 2007 Laser qualification testing of space optics *Proc. SPIE* **6403** 284–90
- [22] Allenspacher P, Riede W and Wernham D 2005 Vacuum laser damage test bench *Proc. SPIE* **5991** 599128–1
- [23] Gingreau C, Lanternier T, Laignère L, Donval T, Courchinoux R, Leymarie C and Néauport J 2018 Impact of mechanical stress induced in silica vacuum windows on laser-induced damage *Opt. Lett.* **43** 1706–9
- [24] Juškevičius K, Buzelis R, Abromavicius G, Samuilovas R, Abbas S, Belosludtsev A, Drazdys R and Kicas S 2017 Argon plasma etching of fused silica substrates for manufacturing high laser damage resistance optical interference coatings *Opt. Mater. Express* **7** 3598
- [25] Oulehla J and Lazar J 2014 Station for LIDT tests of optical components under cryogenic conditions *Proc. SPIE* **9237** 923720
- [26] Kafka K R P, Talisa N, Tempea G, Austin D R, Neacsu C and Chowdhury E A 2016 Few-cycle pulse laser induced damage threshold determination of ultra-broadband optics *Opt. Express* **24** 28858–68
- [27] Mikami K, Motokoshi S, Fujita M, Jitsuno T and Tanaka K A 2011 Laser-induced damage thresholds of optical coatings at different temperature *Proc. SPIE* **8190** 110–6
- [28] Mikami K, Motokoshi S, Somekawa T, Jitsuno T, Fujita M and A K Tanaka 2013 A theoretical analysis for temperature dependences of laser-induced damage threshold *Proc. SPIE* **8885** 88851T
- [29] Bartels N, Allenspacher P and Riede W 2018 Laser conditioning of UV anti-reflective optical coatings for applications in aerospace *Proc. SPIE* **10805** 108051Q
- [30] Avicé J 2018 *Etudes des propriétés physico-chimiques de revêtements sol-gel par spectroscopie, optoacoustique et endommagement laser* Doctoral dissertation Le Mans Université
- [31] Avicé J, Piombini H, Boscher C, Belleville P, Vaudel G, Brotons G and Gusev V 2017 Link between mechanical strength and laser damage threshold for antireflective coating made by sol-gel *Proc. SPIE* **10447** 61–71
- [32] Pommies M, Damiani D, Bertussi B, Capoulade J, Piombini H, Natoli J Y and Mathis H 2006 Detection and characterization of absorption heterogeneities in KH_2PO_4 crystals *Opt. Commun.* **267** 154–61
- [33] Piombini H, Damiani D, Damamme G, Natoli J-Y, Bertussi B and Commandré M 2005 Highlighting of local inhomogeneity in excimer conditioning of KDP *Proc. SPIE* **5647** 279–89
- [34] Damiani D, Piombini H, Plessis D, Donval T, Laignère L and Loiseau M 2005 Excimer laser conditioning of KDP: influence of the laser parameters and crystal orientation on the laser damage threshold *Proc. SPIE* **5647** 290–7
- [35] Pommies M, Damiani D, Bertussi B, Capoulade J, Natoli J Y, Piombini H and Mathis H 2005 Nondestructive optical characterization of KH_2PO_4 crystals heterogeneities and adapted excimer laser conditioning process *Proc. SPIE* **5965** 509–17
- [36] Bertussi B, Piombini H, Damiani D, Pommies M, Le Borgne X and Plessis D 2006 SOCRATE: an optical bench dedicated to the understanding and improvement of a laser conditioning process *Appl. Opt.* **45** 8506–16
- [37] Damiani D Elaboration, mise en forme et caractérisation de matériaux pour l'énergie par interaction rayonnement-matière
- [38] Franta D, Dubroka A, Wang C, Giglia A, Vohánka J, Franta P and Ohlídal I 2017 Temperature-dependent dispersion model of float zone crystalline silicon *Appl. Surf. Sci.* **421** 405–19
- [39] Pilar J, De Vido M, Divoky M, Mason P, Hanus M, Ertel K, Navratil P, Butcher T, Slezak O and Banerjee S 2018 Characterization of Bivoj/DiPOLE 100: HiLASE 100-j/10-hz diode pumped solid state laser *Proc. SPIE* **10511** 120–6
- [40] Muresan M G, Cech P, Bilek V, Horodyska P, Rostohar D, Lucianetti A and Mocek T 2018 Laser induced damage in optical glasses using nanosecond pulses at 1030 nm *Proc. SPIE* **10805** 266–74
- [41] Andrés Zarate E, Edén Custodio G, Treviño-Palacios C G, Rodríguez-Vera R and Hector J 2005 Puga-Soberanes 2005 Defect detection in metals using electronic speckle pattern interferometry *Sol. Energy Mater. Sol. Cells* **88** 217–25
- [42] Marshall J L, Williams P, Rheault J-P, Prochaska T, Allen R D and DePoy D L 2014 Characterization of the reflectivity of various black materials *Proc. SPIE* **9147** 91474F